Electrodynamics on Fermi Cyclides in Nodal Line Semimetals

Seongjin Ahn,[1] E. J. Mele,[2,*] and Hongki Min[1,2,†]
[1]*Department of Physics and Astronomy, Seoul National University, Seoul 08826, Korea*
[2]*Department of Physics and Astronomy, University of Pennsylvania, Philadelphia, Pennsylvania 19104, USA*

(Received 3 March 2017; published 5 October 2017)

We study the frequency-dependent conductivity of nodal line semimetals (NLSMs), focusing on the effects of carrier density and energy dispersion on the nodal line. We find that the low-frequency conductivity has a rich spectral structure which can be understood using scaling rules derived from the geometry of their Dupin cyclide Fermi surfaces. We identify different frequency regimes, find scaling rules for the optical conductivity in each, and demonstrate them with numerical calculations of the inter- and intraband contributions to the optical conductivity using a low-energy model for a generic NLSM.

DOI: 10.1103/PhysRevLett.119.147402

Introduction.—Interest in topological states of quantum matter has led to the identification of new gapless electronic states that support nontrivial geometric structures in their band structures at or near the Fermi energy. In topological semimetals, the conduction and valence bands contact at points or lines in momentum space, and the band degeneracy at the contact is protected by symmetries such as crystalline and time-reversal symmetries. Among the three-dimensional topological semimetals, Weyl (Dirac) semimetals have nondegenerate (degenerate) conduction and valence bands which touch at discrete points, whereas in nodal line semimetals (NLSMs), the two bands cross on closed lines in momentum space [1–4].

When protected by a mirror symmetry, such a nodal line is "flat" in the sense that it lies in a single plane in $\boldsymbol{k}$ space. However, the contact line is not similarly constrained to occur on a constant energy surface. An energy dispersion on the nodal line has no effect on its topological character, which is determined by the phase winding of the Bloch states around the singularity. However, it generically forces the system into a semimetallic state with coexisting electron and hole pockets and an unconventional Fermi surface (FS) geometry, exhibiting the rich structures of Dupin cyclide geometries [5], as shown in Fig. 1. Here the geometry of the FS is determined by a combination of the energy dispersion of the contact line (tilt) and the Fermi energy which play a crucial role in determining various physical properties in NLSMs.

The optical conductivity of a low-energy model for a NLSM in the absence of tilt has recently been studied [6]. However, once an energy tilt is introduced, there is a competition between two energy scales set by the amount of dispersion and by the chemical potential. In this work, we study the consequences of this competition for the low-frequency conductivity of a NLSM and analyze its characteristic frequency dependence using the geometry of the Dupin cyclide. We find new spectral features that occur as a result of its unconventional geometry. For a nonzero Fermi energy smaller than the tilt energy scale, full Pauli blocking is prevented, and instead all three diagonal components of the optical conductivity tensor show linear scaling with frequency. For the Fermi energy larger than the tilt energy,

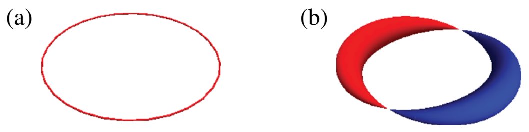

Ring
$\Delta_t = 0, \varepsilon_F = 0$

Symmetric horn cyclide
$\Delta_t \neq 0, \varepsilon_F = 0$

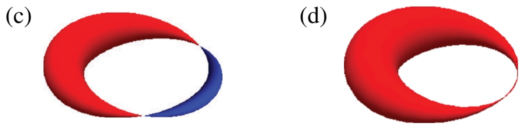

Horn cyclide
$0 < \varepsilon_F < \Delta_t$

Horn cyclide
$0 < \varepsilon_F = \Delta_t$

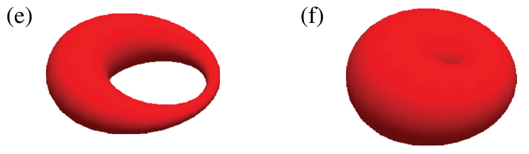

Ring cyclide
$0 < \Delta_t < \varepsilon_F$

Spindle cyclide
$0 < \Delta_t < \varepsilon_F = \varepsilon_0$

FIG. 1. Evolution of the FS as a function of tilt Δ_t and Fermi energy ε_F with red (blue) indicating the electron (hole) pocket. (a) At zero Fermi energy with zero tilt, the FS has a one-dimensional ring shape sitting on the zero-energy plane. (b) With a finite tilt, the ring shape evolves into a symmetric horn cyclide containing both electron and hole pockets symmetrically, which vanish at two contact points. Upon increasing the Fermi energy, the electron and hole pockets (c) become asymmetric and the contact points move out from the symmetrical axis, (d) converge into a single point when the Fermi energy equals the tilt energy, and (e) vanish when the Fermi energy becomes larger than the tilt energy. (f) When the Fermi energy equals the energy scale of the ring radius, the FS is merged into a spherelike shape with no holes in the center, similar to that of Weyl semimetals.

the interband optical conductivity recovers a gap due to Pauli blocking. We find nonanalytic features in both the frequency dependence of the interband conductivity and the chemical potential dependence of the Drude stiffness which arises from Lifshitz transitions of the FS.

Model.—In the continuum approximation, the minimal Hamiltonian for tilted NLSMs that captures the essential features of its low-energy excitations takes the form of a 2 by 2 matrix given by [7,8]

$$H = \hbar v q_\rho \sigma_x + \hbar v k_z \sigma_y + \hbar \boldsymbol{v}_t \cdot \boldsymbol{k} \sigma_0, \tag{1}$$

where σ_x and σ_y are the Pauli matrices, σ_0 is the identity matrix, $\boldsymbol{v}_t$ is the tilt velocity, $q_\rho = k_\rho - k_0$, $k_\rho = \sqrt{k_x^2 + k_y^2}$, and k_0 is the radius of the nodal ring. The eigenenergies of the Hamiltonian are given by

$$\varepsilon_\pm(\boldsymbol{k}) = \pm \hbar v \sqrt{q_\rho^2 + k_z^2} + \hbar \boldsymbol{v}_t \cdot \boldsymbol{k}, \tag{2}$$

which has a ring shape zero-energy contour with a slope of $\boldsymbol{v}_t$. In the following, we consider tilt only in the in-plane direction, because it produces electron-hole pockets, leading to qualitative changes in the optical conductivity, whereas tilt along the perpendicular axis has little effect on the optical conductivity unless it is so extreme that the system is in a type-II semimetallic state [9]. Without the loss of generality, we therefore set $\boldsymbol{v}_t = v_t \hat{x}$.

Remarkably, in toroidal coordinates [9], this NLSM Hamiltonian in Eq. (1) can be written in the same form as the low-energy graphene Hamiltonian, but expressed in polar coordinates (r, θ) centered at $\boldsymbol{k}_0$ [see Fig. 2(a)]:

$$H = \varepsilon_0 \begin{pmatrix} 0 & \tilde{r} e^{-i\theta} \\ \tilde{r} e^{i\theta} & 0 \end{pmatrix} + \Delta_t (1 + \tilde{r} \cos\theta) \cos\phi \sigma_0, \tag{3}$$

where $\tilde{r} = r/k_0$, $\varepsilon_0 = \hbar v k_0$, and $\Delta_t = \hbar v_t k_0$. Thus, in the energy range where the toroidal structure is maintained, we can consider NLSMs as a collection of graphene sheets with tilt in the x direction and the Dirac point shifted from zero energy by $\Delta_t \cos\phi$ [see Fig. 2(b)].

Optical conductivity obtained from a collection of graphene sheets.—In the linear response limit, we obtain the optical conductivity of NLSMs by summing up individual contributions from each of the graphene sheets:

$$\sigma_{ii}^{\mathrm{NLSM}} = k_0 \int_0^{2\pi} \frac{d\phi}{2\pi} \sigma^{\mathrm{gr}}(\phi) \mathcal{F}_{ii}(\phi), \tag{4}$$

where $i = x,\ y,\ z$, $\sigma^{\mathrm{gr}}(\phi)$ is the optical conductivity of a graphene sheet located at ϕ with tilt in the x direction, and $\mathcal{F}_{xx}(\phi) = \cos^2\phi$, $\mathcal{F}_{yy}(\phi) = \sin^2\phi$, $\mathcal{F}_{zz}(\phi) = 1$ are geometric factors from the projection of an external electric field on the graphene sheet and that of the in-plane velocity of graphene on the current direction. Note that Eq. (4) is valid for $\hbar\omega < 2\varepsilon_0$ where the toroidal structure is maintained.

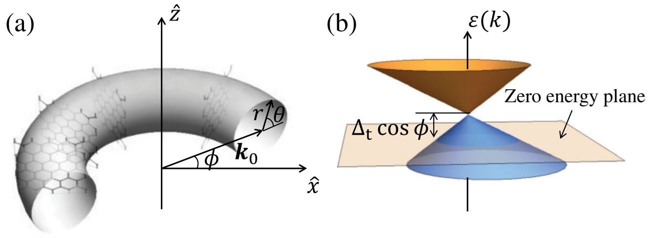

FIG. 2. (a) Schematic illustration of toroidal coordinates and graphene sheets standing perpendicular to the nodal-line plane. (b) The Dirac cone energy dispersion of the graphene sheet located at ϕ. Note that the Dirac cone is shifted from the zero energy by $\Delta_t \cos\phi$.

First, consider the case of $\Delta_t = 0$. Since the optical conductivity from a single Dirac cone filled to energy ε_F is given by $\sigma^{\mathrm{gr}}(\phi) = (e^2/16\hbar)\Theta(\hbar\omega - 2|\varepsilon_F|)$ [12], the optical conductivity of the NLSM is

$$\frac{\sigma_{ii}}{\sigma_0} \approx \begin{cases} \frac{1}{2}\Theta(\hbar\omega - 2|\varepsilon_F|) & \text{for } i = x, y, \\ \Theta(\hbar\omega - 2|\varepsilon_F|) & \text{for } i = z, \end{cases} \tag{5}$$

where $\sigma_0 = e^2 k_0/16\hbar$. Thus, for $\hbar\omega < 2|\varepsilon_F|$ the optical conductivity vanishes due to Pauli blocking, whereas for $2|\varepsilon_F| < \hbar\omega < 2\varepsilon_0$ it remains constant [6].

For $\Delta_t \neq 0$, the conductivity should be modified to take into account (i) the shift of the Dirac point from zero energy [first term of σ_0 in Eq. (3)] and (ii) the tilted linear band dispersion (second term). At low frequencies ($\hbar\omega \ll \varepsilon_0$), however, when the Dirac points lie close to zero energy, the tilt in the band dispersion is negligible. Thus, $\sigma_{ii}(\omega)$ at low frequencies can be obtained using $\sigma^{\mathrm{gr}}(\phi) \approx (e^2/16\hbar)\Theta(\hbar\omega - 2|\varepsilon_F - \Delta_t \cos\phi|)$ in Eq. (4), giving

$$\frac{\sigma_{ii}}{\sigma_0} \approx \int_0^{2\pi} \frac{d\phi}{2\pi} \Theta(\hbar\omega - 2|\varepsilon_F - \Delta_t \cos\phi|) \mathcal{F}_{ii}(\phi). \tag{6}$$

In the following, we present numerically calculated optical conductivities over a wide frequency range in the presence of tilt and finite Fermi energy by evaluating the Kubo formula [see Eq. (6) in Supplemental Material [9]]. We analyze the results by investigating the geometry of the phase space (PS) for interband transitions and the low-frequency analytic forms obtained from Eq. (6). Here, the PS for interband transitions is given by the intersection between the outside of the FS and the PS allowed by energy conservation. For a given frequency ω, the PS for NLSMs allowed by energy conservation is the surface of the momentum space torus which satisfies $\hbar\omega = \varepsilon_+(\boldsymbol{k}) - \varepsilon_-(\boldsymbol{k})$.

Optical conductivity with $\varepsilon_F = 0$.—We first consider the case where $\varepsilon_F = 0$ in the presence of tilt. Figures 3(a) and 3(b) show calculated optical conductivities with tilt energies of $\Delta_t = 0.3\varepsilon_0$ and $\Delta_t = 0.6\varepsilon_0$, respectively.

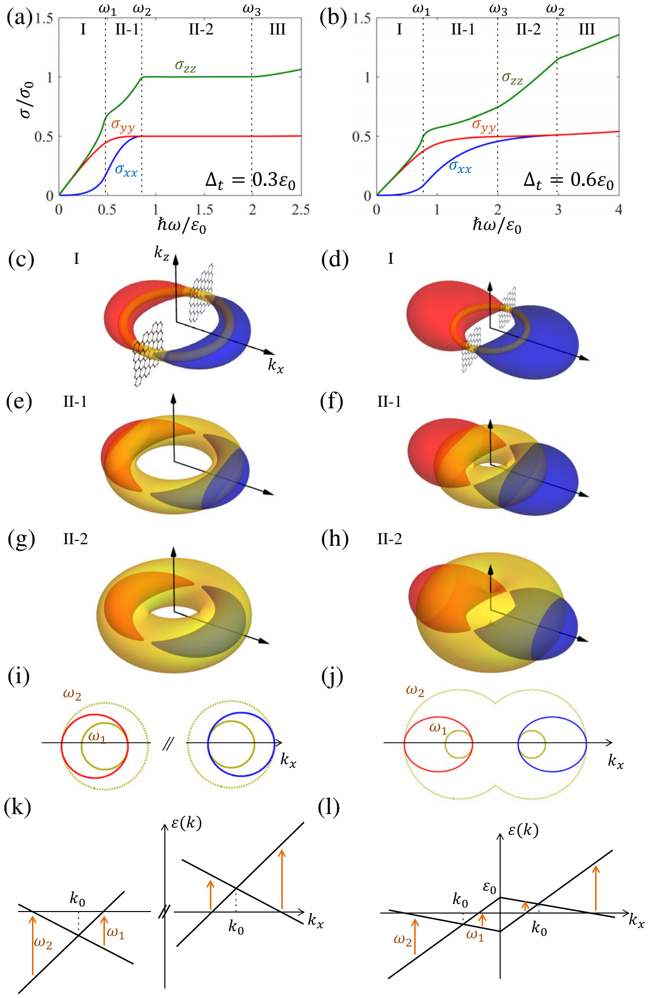

FIG. 3. (a),(b) Calculated optical conductivities of NLSMs for $\varepsilon_F = 0$ with two different tilt energies of (a) $\Delta_t = 0.3\varepsilon_0$ and (b) $\Delta_t = 0.6\varepsilon_0$. Regions I, II-1, II-2, and III represent the frequency domains in which the PS for interband transitions grows continuously without any abrupt changes. (c)–(h) The PS allowed by energy conservation indicated by a yellow torus along with electron (red) and hole (blue) pockets in different frequency domains. Note that in region I the PS allowed for interband transitions consists of two local domains, while in region II they merge together to form a connected geometry. (i),(j) Cross-sectional views of the electron-hole pockets and the PS allowed by energy conservation in the $k_x - k_z$ plane at the frequencies of $\omega = \omega_1$ (yellow solid lines) and $\omega = \omega_2$ (yellow dashed lines), where the PS allowed for interband transitions changes its geometry leading to kink structures in the optical conductivity. (k),(l) Energy band dispersions along the k_x axis with $k_y = k_z = 0$ for (k) $\Delta_t = 0.3\varepsilon_0$ and (l) $\Delta_t = 0.6\varepsilon_0$. The geometrical changes occur at frequencies corresponding to the onset of interband transitions indicated by arrows.

Note that the optical conductivities show kink structures at transitions between different frequency domains (I, II, and III) and characteristic frequency dependences determined by the tilt energies.

In region I, the optical conductivity in the tilt direction is $\sigma_{xx} \propto \omega^3$ at low frequencies, while those in the other directions (σ_{yy} and σ_{zz}) are $\propto\omega$ [see region I in Figs. 3(a) and 3(b)]. Figures 3(c) and 3(d) show the corresponding PS for interband transitions, which is divided into two separated islands located at $\phi = \pm(\pi/2)$. As demonstrated above in Eq. (6), we can express the optical conductivity by averaging contributions from the graphene sheets that occupy these two isolated regions. In the low-frequency limit, in the vicinity of the contact points, the optical conductivity is approximately given by

$$\frac{\sigma_{ii}}{\sigma_0} \approx \int_{\phi\sim\pm\pi/2} \frac{d\phi}{2\pi}\Theta(\hbar\omega - 2|\Delta_t\cos\phi|)\mathcal{F}_{ii}(\phi)$$
$$\approx \frac{2}{\pi}\int_0^{\hbar\omega/2\Delta_t} d\phi\mathcal{F}_{ii}\left(\phi + \frac{\pi}{2}\right). \tag{7}$$

With the expansion of $\mathcal{F}_{ii}(\phi + \pi/2)$ around $\phi = 0$, the resulting conductivities in the lowest order are

$$\frac{\sigma_{ii}}{\sigma_0} = \begin{cases} \frac{1}{12\pi}\left(\frac{\hbar\omega}{\Delta_t}\right)^3 & \text{for } i = x, \\ \frac{\hbar\omega}{\pi\Delta_t} & \text{for } i = y, z, \end{cases} \tag{8}$$

which agree with our numerical results.

At the intersection between regions I and II-1, the PS allowed by energy conservation (yellow torus) begins to touch the boundary of electron (red) and hole (blue) pockets, and the two isolated PS regions for interband transitions merge, forming a connected geometry distinguished from that in region I [see Figs. 3(e) and 3(f)]. Note that this change of geometry produces a kink in σ_{ii} seen most clearly in σ_{zz} because of its ϕ-independent projection factor [$\mathcal{F}_{zz}(\phi) = 1$; see Eq. (4)]. Such a geometrical change also occurs at the intersection between regions II-1 and II-2, giving a kink in σ_{zz}. By observing the cross-sectional view of the PS allowed by energy conservation and the FS in the $k_x - k_z$ plane [see Figs. 3(i) and 3(j)], we can calculate the frequencies at which kinks appear. Alternatively, since the geometrical changes associated with additional interband transitions occur along the k_x axis, the problem of finding kink frequencies is reduced to obtaining ω_1 and ω_2 in Figs. 3(k) and 3(l): $\hbar\omega_1 = [2\Delta_t/(\varepsilon_0 + \Delta_t)]\varepsilon_0$, $\hbar\omega_2 = [2\Delta_t/(\varepsilon_0 - \Delta_t)]\varepsilon_0$.

In region II-2, for $\Delta_t = 0.3\varepsilon_0$, the PS allowed by energy conservation [yellow torus in Fig. 3(g)] covers the whole FS while keeping its toroidal structure similar to the untilted case; thus, the optical conductivity shows flat behavior with exactly the same height as that of untilted NLSMs. For $\Delta_t = 0.6\varepsilon_0$, however, the PS allowed by energy conservation [yellow spherelike manifold in Fig. 3(h)] is no longer a torus and does not fully cover the whole FS, exhibiting a monotonic increase in σ_{zz} instead of the flat behavior. Note that the PS allowed by energy conservation changes its geometry from a torus to a spherelike manifold at the frequency $\hbar\omega_3 = 2\varepsilon_0$. Thus, the condition for the existence (absence) of the flat region can

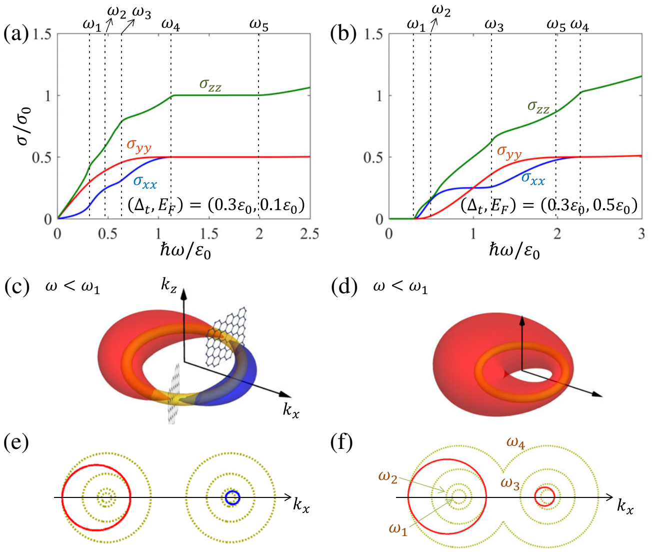

FIG. 4. (a),(b) Calculated optical conductivities of tilted NLSMs with $\Delta_t = 0.3\varepsilon_0$ for two different Fermi energies of (a) $\varepsilon_F = 0.1\varepsilon_0$ and (b) $\varepsilon_F = 0.5\varepsilon_0$. (c),(d) The PS allowed by energy conservation indicated by a yellow torus along with electron (red) and hole (blue) pockets in the low-frequency domain for (c) $\varepsilon_F = 0.1\varepsilon_0$ and (d) $\varepsilon_F = 0.5\varepsilon_0$. (e),(f) Cross-sectional views of the electron-hole pockets and the PS allowed by energy conservation in the $k_x - k_z$ plane at frequencies where kinks appear in the optical conductivity.

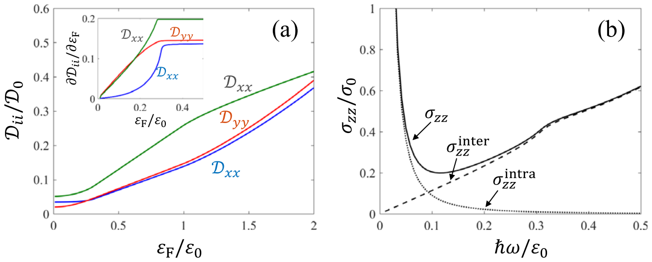

FIG. 5. (a) The Drude weight of tilted NLSMs with $\Delta_t = 0.3\varepsilon_0$ and (b) the intraband ($\sigma_{zz}^{\rm intra}$, dotted line) and interband ($\sigma_{zz}^{\rm inter}$, dashed line) contributions to the optical conductivity σ_{zz} (solid line). The inset in (a) shows the derivative of the Drude weight near $\varepsilon_F = \Delta_t$, where the Drude weight exhibits a nonanalytic kink behavior due to an abrupt change in the geometry of the FS. Here $\mathcal{D}_0 = (e^2/\hbar)k_0\varepsilon_0$, and the Drude weight is defined to be $\sigma_{ii}^{\rm intra} = \mathcal{D}_{ii}\delta(\hbar\omega)$. For (b), we use a finite broadening term $\eta = 0.001\varepsilon_0$ replacing the 0^+ term in Eq. (6) in [9].

be obtained from the condition $\omega_2 < \omega_3$ ($\omega_2 > \omega_3$), leading to $\Delta_t < 0.5\varepsilon_0$ ($\Delta_t > 0.5\varepsilon_0$).

In region III, the PS allowed by energy conservation for both $\Delta_t = 0.3\varepsilon_0$ and $\Delta_t = 0.6\varepsilon_0$ merge into a spherelike geometry covering the whole FS, similar to that of Weyl semimetals. Thus, at high frequencies in this frequency domain, the optical conductivity shows a linear behavior, as already shown in previous studies [6].

Optical conductivity with $\varepsilon_F \neq 0$.—Next, we consider the case where $\varepsilon_F \neq 0$ in the presence of tilt. Figures 4(a) and 4(b) show calculated optical conductivities of NLSMs for $\varepsilon_F = 0.1\varepsilon_0$ and $\varepsilon_F = 0.5\varepsilon_0$, respectively, with $\Delta_t = 0.3\varepsilon_0$. At low frequencies, the optical conductivity for $\varepsilon_F = 0.1\varepsilon_0$ increases linearly with increasing ω, whereas that for $\varepsilon_F = 0.5\varepsilon_0$ exhibits an optical gap.

To address the difference in the low-frequency behaviors, in Figs. 4(c) and 4(d) we show the PS allowed by energy conservation corresponding to a low-frequency range along with electron-hole pockets. For $\varepsilon_F = 0.1\varepsilon_0$, there is an available PS for interband transitions consisting of two separate local domains located around the contact points between the electron and hole pockets. Similarly as we did for $\varepsilon_F = 0$, after replacing $|\Delta_t \cos\phi|$ with $|\varepsilon_F - \Delta_t \cos\phi|$ in Eq. (7), we obtain the low-frequency optical conductivity as $\sigma_{ii}/\sigma_0 \approx C_i(\hbar\omega/\pi\Delta_t)$, where $i = x$, y, z, $\phi_0 = \cos^{-1}(\varepsilon_F/\Delta_t)$ is the location of graphene sheets sitting around the PS for interband transitions, $C_x = [(\varepsilon_F/\Delta_t)^2/\sqrt{1-(\varepsilon_F/\Delta_t)^2}]$, $C_y = \sqrt{1-(\varepsilon_F/\Delta_t)^2}$, and $C_z = [1/\sqrt{1-(\varepsilon_F/\Delta_t)^2}]$. Note that, in the presence of finite ε_F, the linear term dominates over the cubic one in the optical conductivity along the tilt direction, in contrast to the $\varepsilon_F = 0$ case [see Eq. (7)]. (For $\varepsilon_F = \Delta_t$ case, see Sec. III in Ref. [9]).

For $\varepsilon_F = 0.5\varepsilon_0$, there is no available PS for interband transitions at low frequencies, because the electron pocket becomes large enough to cover the entire PS allowed by energy conservation, leading to an optical gap due to Pauli blocking [see Fig. 4(d)]. The optical gap persists up to the frequency where the PS allowed by energy conservation touches the boundary of the electron pocket. Similarly as in the $\varepsilon_F = 0$ case, we can obtain the size of the optical gap to be $\hbar\omega_{\rm gap} = 2[(\varepsilon_F - \Delta_t)/(\varepsilon_0 + \Delta_t)]\varepsilon_0$ and thus the condition for the existence of an optical gap: $\varepsilon_F > \Delta_t$.

As ε_F increases, the electron (hole) pocket grows (shrinks), because the number of electrons in the system increases. The imbalanced sizes of the electron and hole pockets lead to two more kinks compared with the $\varepsilon_F = 0$ case, as shown in Figs. 4(e) and 4(f). Similarly as in the $\varepsilon_F = 0$ case, we can obtain $\hbar\omega_1 = 2|(\varepsilon_F - \Delta_t)/(\varepsilon_0 + \Delta_t)|\varepsilon_0$, $\hbar\omega_2 = 2|(\varepsilon_F - \Delta_t)/(\varepsilon_0 - \Delta_t)|\varepsilon_0$, $\hbar\omega_3 = 2|(\varepsilon_F + \Delta_t)/(\varepsilon_0 + \Delta_t)|\varepsilon_0$, and $\hbar\omega_4 = 2|(\varepsilon_F + \Delta_t)/(\varepsilon_0 - \Delta_t)|\varepsilon_0$. It follows that the condition for the existence of a flat region can be obtained from $\hbar\omega_4 > \hbar\omega_5 \equiv 2\varepsilon_0$, leading to $\Delta_t < \frac{1}{2}(\varepsilon_0 - \varepsilon_F)$ [9]. Here ω_5 is the frequency where the PS allowed by energy conservation changes its geometry from a torus to a spherelike manifold.

The intraband contribution to optical conductivity gives rise to a Drude peak at low frequencies whose weight also inherits a nonanalytic density dependence from the geometry of the FS. Interestingly, these are seen most clearly in the *derivatives* of the weight with respect to Fermi energy, as shown in Fig. 5.

Discussion.—Introducing spin-orbit coupling (SOC) can gap out a nodal line and produce pairs of Weyl points [8].

In such cases, at frequencies below the SOC scale, the PS for interband transitions are spheres enclosing the Weyl nodes, and the conductivity will revert to linear frequency scaling known for Weyl semimetals (WSMs). Above the SOC energy, however, the separated PS recovers a toroidal shape, and this will have the characteristic dependence found in our work. Recent calculations for WSMs in the TaAs class indicate that these materials are weakly broken line node systems where the tilt scale dominates the SOC scale [13]. Thus, our analysis is applicable over a wide frequency range and can be used as a signature of these new states of matter in optical experiments.

We thank A. Bansil for communicating unpublished data on the band structure of WSMs in the TaAs family. This research was supported by the Basic Science Research Program through the National Research Foundation of Korea (NRF) funded by the Ministry of Education under Grant No. 2015R1D1A1A01058071. E. J. M.'s work on this project was supported by the U.S. Department of Energy, Office of Basic Energy Sciences under Award No. DE-FG02-ER45118. H. M. acknowledges travel support provided by the University Research Foundation at the University of Pennsylvania while this work was carried out.

---

[*] mele@physics.upenn.edu
[†] hmin@snu.ac.kr

[1] A. A. Burkov, M. D. Hook, and Leon Balents, Topological nodal semimetals, Phys. Rev. B **84**, 235126 (2011).

[2] C.-K. Chiu and A. P. Schnyder, Classification of reflection-symmetry-protected topological semimetals and nodal superconductors, Phys. Rev. B **90**, 205136 (2014).

[3] C. Fang, H. Weng, X. Dai, and Z. Fang, Topological nodal line semimetals, Chin. Phys. B **25**, 117106 (2016).

[4] R. Yu, Z. Fang, X. Dai, and H. Weng, Topological nodal line semimetals predicted from first-principles calculations, Front. Phys. **12**, 127202 (2017).

[5] L. P. Eisenhart, *A Treatise on the Differential Geometry of Curves and Surfaces* (Dover, New York, 1960).

[6] J. P. Carbotte, Optical response of a line node semimetal, J. Phys. Condens. Matter **29**, 045301 (2017).

[7] K. Mullen, B. Uchoa, and D. T. Glatzhofer, Line of Dirac Nodes in Hyperhoneycomb Lattices, Phys. Rev. Lett. **115**, 026403 (2015).

[8] C. Fang, Y. Chen, H.-Y. Kee, and L. Fu, Topological nodal line semimetals with and without spin-orbital coupling, Phys. Rev. B **92**, 081201(R) (2015).

[9] See Supplemental Material at http://link.aps.org/supplemental/10.1103/PhysRevLett.119.147402 for details of the toroidal coordinate transformation, the Kubo formula for optical conductivity, low-frequency asymptotic forms in the presence of tilt and Fermi energy, a phase diagram for the existence of an optical gap and a flat region, a comparison with other models, and optical conductivity with different forms of tilt, which includes Refs. [10,11].

[10] G. D. Mahan, *Many-Particle Physics*, 3rd ed. (Springer, New York, 2000).

[11] M. Koshino and I. F. Hizbullah, Magnetic susceptibility in three-dimensional nodal semimetals, Phys. Rev. B **93**, 045201 (2016).

[12] T. Ando, Y. Zheng, and H. Suzuura, Dynamical conductivity and zero-mode anomaly in honeycomb lattices, J. Phys. Soc. Jpn. **71**, 1318 (2002).

[13] A. Bansil (private communication).